Check for updates

ChemCatChem

Research Article
doi.org/10.1002/cctc.202500419

Chemistry Europe
European Chemical Societies Publishing

www.chemcatchem.org

Graphitic Carbon Nitride/Nickel Oxide/Pt Heterojunction Photocatalysts for Hydrogen Production from Ammonia Borane Under White-Light Irradiation

Sibel Eken Korkut,*[a, b] Merve Aksoy,[a, c] and Önder Metin*[a, c, d]

Graphitic carbon nitride/Nickel oxide-X (gCN/NiO-X, where X represents the Ni wt%) binary heterojunctions were synthesized using a simple method and then platinum nanoparticles (Pt NPs) were then in situ generated on the gCN/NiO-X binary heterojunctions by reducing the pre-anchored Pt ions during the hydrolysis of ammonia borane (HAB) under white-light irradiation. The gCN/NiO-3.12%/Pt(IV) heterojunctions, with 1.31 wt% Pt, exhibited the highest turnover frequency (TOF) of 132.9 mol H_2 mol Pt^{-1} min^{-1} in hydrogen generation from AB hydrolysis, which is 1.9 times higher than that of gCN/Pt(IV) nanocomposites. The enhanced activity of the gCN/NiO/Pt nanocatalysts can be attributed to the heterojunction formed between gCN and NiO, which facilitates greater visible-light absorption, more efficient photo-induced charge separation, and improved charge carrier transfer compared to the gCN/Pt nanocatalysts in photo-assisted HAB. Reusability tests demonstrated that the gCN/NiO/Pt heterojunction photocatalysts retained 84% of their initial hydrogen generation rate (mL H_2/min) after five consecutive runs of HAB. For the first time, this study demonstrates that the gCN/NiO binary heterojunctions are easily synthesized and to be preferred as the photoactive support materials for the in situ growth of Pt NPs as catalysts for not only hydrogen generation but also other chemical transformations.

1. Introduction

Due to the current energy related problems such as source depletions and environmental impacts of carbon emission, the sustainable energy production, storage, and utilization are very crucial for realizing a greener future.[1] Hydrogen (H_2) has emerged as a highly efficient energy vector, attributed to its potential to revolutionize various sectors owing to its clean and abundant nature, high energy density, and zero-emission properties.[2] However, one of the major ongoing challenges associated with the hydrogen energy lies in its storage. Hydrogen is the lowest density gas at ambient conditions and compressing it to a sufficient density for a practical storage can be challenging and energy consuming due to the required specialized storage infrastructure and materials to ensure safety and prevent losses, especially for the mobility applications.[3] Hydrogen can be stored either physically or chemically, depending on its form-whether as hydrogen gas (H_2) or combined with other elements (such as B, C, N, etc.) in hydridic or protonic forms to create a wide range of chemical compounds. Physical hydrogen storage technology can be categorized into three main methods: compressed gaseous hydrogen, liquid hydrogen under cryo-conditions, and adsorption on large surface area materials such as metal-organic frameworks (MOFs), zeolites, polymers with intrinsic microporosity, and carbon materials. However, none of these physical methods are yet affordable, lightweight, or sufficiently safe to unlock hydrogen's full potential for enabling decarbonized economies.[4] In contrast, chemical hydrogen storage methods, using solid compounds (such as metal hydrides, complex hydrides, amides, imides, ammineborane adducts, etc.) and liquid hydrogen storage materials (liquid organic hydrogen carriers, hydrazine, formic acid, etc.) offer higher volumetric and gravimetric hydrogen densities, minimized potential risk, and reduced capital investment, which is mainly due to their greater compatibility with existing transport infrastructure compared to physical storage methods.[5] Among the addressed various methods for chemical hydrogen storage, ammonia borane (H_3NBH_3, AB) has emerged as a promising candidate as being a solid compound having high hydrogen density (19.6 wt%), low molecular weight (30.9 g/mol), and stability in aqueous solution, making it an advantageous option for efficient

[a] Assist. Prof. Dr. S. E. Korkut, Dr. M. Aksoy, Prof. Dr. Ö. Metin
Department of Chemistry, College of Sciences, Koç University, Istanbul 34450, Turkey
E-mail: seken@yildiz.edu.tr
ometin@ku.edu.tr

[b] Assist. Prof. Dr. S. E. Korkut
Department of Chemistry, Faculty of Arts and Sciences, Yıldız Technical University, Istanbul 34349, Turkey

[c] Dr. M. Aksoy, Prof. Dr. Ö. Metin
Koç University TÜPRAŞ Energy Center (KUTEM), Istanbul 34450, Turkey

[d] Prof. Dr. Ö. Metin
Koç University Surface Science and Technology Center (KUYTAM), Istanbul 34450, Turkey

Sibel Eken Korkut and Merve Aksoy contributed equally to this work.

Supporting information for this article is available on the WWW under https://doi.org/10.1002/cctc.202500419

© 2025 The Author(s). ChemCatChem published by Wiley-VCH GmbH. This is an open access article under the terms of the Creative Commons Attribution-NonCommercial License, which permits use, distribution and reproduction in any medium, provided the original work is properly cited and is not used for commercial purposes.

© 2025 The Author(s). ChemCatChem published by Wiley-VCH GmbH

chemical hydrogen storage.[6] However, in its pristine form, AB has limited hydrogen release kinetics and it requires an appropriate catalyst, such as transition metal complex or heterogeneous catalyst, to accelerate the hydrolysis process significantly in a controlled way of hydrogen release.[7] Researchers are actively exploring different catalyst systems with some optimization strategies to improve the efficiency of hydrogen production rate and the stability such that AB holds a great promise for enabling practical and efficient hydrogen storage, contributing to the large-scale utilization of hydrogen as an environmentally friendly and renewable energy source.[8]

Over the past years, there has been growing interest in utilizing photocatalysts for the hydrolysis of AB (hydrolysis of ammonia borane (HAB) will be used hereafter), offering a sustainable and environmentally friendly approach to improve the efficiency and kinetics of HAB.[9–11] The studies have shown that the integration of heterojunction structures into the photocatalytic systems can significantly enhance the catalytic performance due to the acquired efficient charge separation and transportation, in general.[12] Various semiconductors with suitable band properties have been explored as a component for the construction of efficient heterojunctions.[13] Among these heterosystems, especially graphitic carbon nitride (gCN)-based ones, which are the combination of gCN with a wide range of available semiconductors such as single metal oxides (sulfides),[14,15] composite metal oxides,[16,17] metal halides,[18,19] and carbon based layered nanomaterials,[20,21] have been widely studied to enable more effective utilization of light energy and enhance electron/hole transport capabilities of gCN. Therefore, the unique advantages of gCN, including physicochemical stability, favorable electronic structure with a band gap of 2.7 eV, 2D layered structure, and easy synthesis via one-step polymerization are further extended,[22] which make gCN based heterostructures favorite materials in various photocatalytic applications such as hydrogen evolution,[23,24] dye decomposition,[25] CO_2 conversion,[26,27] water disinfection,[28] and organic transformations.[29] For the design of effective photocatalysts in the photocatalytic HAB, the semiconductor properties of gCN were generally combined with its role as being a very useful support material for the construction of metal/gCN Mott-Schottky heterojunctions (mpg-C_3N_4@AgPd,[30] mpg-CN/Pt,[31] Co/g-C_3N_4, FeCo/ g-C_3N_4, CuCo/ g-C_3N_4,[32] gCN/Au_xPt_{100-x},[33] Co/P_xCN,[34] and Co/PCN[35]) and an enhancement in the photocatalytic activity is observed to some extent. Additionally, the optimized gCN/semiconductor heterojunction structures were employed as the photoactive support materials to deposit metal NPs acting as the electron-rich active sites. As one of the first studies, Korkut et al. introduced the mesoporous g-C_3N_4/black phosphorus binary heterojunctions as effective photoactive support materials, providing improved catalytic activity to the anchored AgPd alloy NPs in AB methanolysis under light irradiation, due to the gained broaden visible-light response and the prolonged charge carrier lifetime of g-C_3N_4 via hybridization.[36] Wei et al. closely related the high activity of Ru/CdS/C_3N_4 photocatalyst to the outstanding performance of the CdS/C_3N_4 heterojunctions that enable the extended the light absorption edge of CdS/C_3N_4 to 540 nm and enhanced lifetime of the photoexcited charge carriers, which promotes the catalytic activity of Ru NPs.[37] Similarly, our group reported gCN/a-WO_x/Pt nanocatalysts, including heterojunction between gCN and amorphous tungsten oxides species in multiple oxidation states (a-WO_x), enhanced the charge kinetics and absorption abilities of gCN together with a reduction in the band gap.[38] Moreover, we demonstrated that the in-situ formation of Pt NPs on gCN/a-WOx nanocomposites exhibited much better HAB activity than Pt NP growth on pristine gCN under white light irradiation.[38] As also emphasized in the paper, the incorporation of transition metal oxides to the multicomponent systems is one of the most important strategies for the efficient structural of metal nanocatalysts in the HAB. This is because the rate-determining step in the metal catalyzed HAB is the dissociation of H from the H—OH bond in H_2O, which can be catalyzed by transition metal oxides that can readily enhance the adsorption of H—OH on their surface and dissociates electropositive H for attacking the electronegative H in AB.[39] In this regard, Ren et al. reported that the heterostructured NiO/Ni NPs as a support material made a unique contribution to the catalytic performance of Pt nanoclusters in the HAB due to the promoted adsorption and H—OH bond cleavage of H_2O and the generation of an electron-enriched Pt surface via the promotion of NiO and Ni, respectively, of which together maximize the electron interaction and synergic effect in the Pt@NiO/Ni-CNT hybrid nanocatalysts.[40] However, the potential of nickel oxide (NiO) decorated gCN heterostructures (gCN/NiO) in the HAB remains unexplored even though they have shown a great promise in many photocatalytic applications.[41–43]

This study aims to achieve the formation of gCN/NiO nanocomposites and examine their roles as being both an effective heterojunction structures and support materials for the in-situ synthesis of Pt NPs during HAB under white-light irradiation. For this purpose, a facile synthesis procedure was applied to gain gCN/NiO heterojunctions with different Ni contents. Next, in-situ synthesis of Pt nanoparticles along with HAB were realized on each nanocomposite to measure Ni wt% dependent photocatalytic activity and select the optimized condition. Based on the characterization results of the nanocomposites, the photocatalytic activity results were discussed and interpreted in detail.

2. Experimental Section

2.1. Synthesis of gCN/NiO Nanocomposites

gCN was synthesized by heating melamine in muffle furnace under atmospheric condition by following a well-known thermal polycondensation protocol.[44] In a typical synthesis of gCN, 4.0 g of melamine was placed in a porcelain crucible protected with a lid. The temperature was increased from 25 to 550 °C at the rate of 3 °C/min, then hold at 550 °C for 4 h, and lowered to 25 °C by just letting furnace cool down. A yellow powder of ca. 2.0 g of gCN was obtained. According to this amount of gCN obtained, the required amount of $NiCl_2.6H_2O$ salt, which were added to synthesize gCN/NiO nanocomposites with different Ni content, was calculated. It was found to be about 161.9, 242.9, 323.9, and 485.9 mg $NiCl_2.6H_2O$ salt which should be added to get theoretically 2, 3, 4, 6 wt% Ni loaded gCN/NiO nanocomposites. The gCN/NiO nanocomposites with dif-

© 2025 The Author(s). ChemCatChem published by Wiley-VCH GmbH

18673899, 2025, 14, Downloaded from https://chemistry-europe.onlinelibrary.wiley.com/doi/10.1002/cctc.202500419 by Koc University, Wiley Online Library on [13/11/2025]. See the Terms and Conditions (https://onlinelibrary.wiley.com/terms-and-conditions) on Wiley Online Library for rules of use; OA articles are governed by the applicable Creative Commons License

ferent amount of Ni were prepared by mixing the 4.0 g of melamine with solutions of nickel chloride, prepared by dissolving the required amounts of $NiCl_2.6H_2O$ in 6 mL of DI water. The resulting suspension was mixed gently for 4 hours, hold in the oven at 80 °C until drying, and calcined for 4 hours at 550 °C in muffle furnace by following the same heating procedure to get the pristine gCN, explained above. Following cooling down to room temperature, the powders were moved away from the furnace and washed with DI water to remove the impurities, such as chloride ions or uncoupled Ni derivates, from the surface of gCN/NiO composites. As the Ni content (0–6 wt%) in the composites is increased, the change in the color of the composites, from yellow to brown, becomes sharper.

2.2. Synthesis of gCN/NiO/Pt Nanocatalysts During the AB Hydrolysis (HAB)

The synthesized gCN/NiO nanocomposites with different Ni contents were used as support materials to synthesize gCN/NiO/Pt nanocatalysts. Initially, 50 mg of gCN/NiO nanocomposites were subjected to sonication in 20 mL of ethanol inside an ultrasonic bath for 1 h. Subsequently, a specific quantity of hexachloroplatinic acid hexahydrate ($H_2PtCl_6.6H_2O$) dissolved in deionized water was added dropwise to the gCN/NiO dispersion, while maintaining sonication conditions. The resulting solution was further sonicated for 3 h and then left for overnight stirring. Finally, the solvent was removed via centrifugation at 9000 rpm for 10 min and the collected catalyst washed twice with ethanol by following the same centrifugation procedure. The obtained powder was vacuum dried at 50 °C, yielding gCN/NiO/Pt(IV) nanocomposites with a theoretical Pt loading of 2 wt%. After that, 10 mg of the obtained gCN/NiO/Pt(IV) nanocomposites were sonicated in 8 mL of DI water and transferred into a two-necked jacketed glass reactor, connected to a water-filled burette system employed to determine the H_2 production during HAB. The reactor was also connected to a circulating water bath to maintain a constant temperature of 25 ± 0.5 °C throughout the reaction. A 150 W discharge lamp emitting broad spectrum of wavelengths (340–800 nm) was used as white-light source. The reaction vessel together with the lamp were introduced into a home-made mirror box to make effective use of the light. By quick addition of AB solution, including 30.8 mg AB dissolved in 2 mL H_2O, with a syringe, H_2 generation immediately started, and it was monitored over time according to the displacement of water level in burette system. It was observed that the color of the gCN/NiO/Pt(IV) nanocomposites turned to the light or dark brown rapidly, according to their initial Ni content. After the reaction, the gCN/NiO/Pt nanocatalysts were collected via centrifugation (8500 rpm, 12 min), washed twice with water:ethanol (4:1 v/v ratio) mixture using the same centrifugation procedure, and overnight dried in a vacuum furnace at 50 °C. It was observed that the color of the gCN/NiO/Pt(IV) nanocomposites turn to the light or dark brown according to their initial Ni content.

2.3. Scavenger Experiments

Sodium bicarbonate ($NaHCO_3$) and isopropanol were employed as hole and hydroxyl radical scavengers, respectively, in accordance with the previous studies.[38,45] For these experiments, 10 mg of gCN/NiO/Pt(IV) nanocomposite was dispersed in the reaction solution and then the mixture of scavenger and AB was injected, so that the final concentration of scavenger was fixed at 1.0 mol L^{-1}, which is ten times the concentration of AB (0.1 mol L^{-1}). All experiments were conducted at 25 °C under white-light irradiation. Hydrogen evolution was initiated upon the addition of AB/scavenger solution and monitored by the water-filled burette system.

2.4. Reusability Tests

The reusability of gCN/NiO/Pt nanocatalysts for the HAB was assessed by conducting five consecutive cycles under white-light illumination at room temperature. Once hydrogen generation was completed, the solid catalyst was separated from the reaction solution via centrifugation (8500 rpm, 12 min). The collected catalyst was cleansed with water:ethanol (4:1 v/v ratio) mixture by using the same centrifugation procedure. To prepare for the next cycle, the gathered solid catalyst was re-dispersed by sonicating in DI water for 20 min. The subsequent run of HAB was initiated by adding the same amount of AB solution.

3. Results and Discussion

The consecutive synthesis of the gCN/NiO, gCN/NiO/Pt(IV), and gCN/NiO/Pt samples was summarized in Figure 1. The characterization of gCN/NiO nanocomposites before and after Pt deposition were carried out and the results were discussed in detail. According to XRF (X-ray fluorescence) measurement results, theoretically 2, 3, 4, and 6 wt% Ni loaded gCN/NiO nanocomposites were found to be including experimentally 1.97, 3.12, 3.78, and 5.36% Ni, respectively, as depicted in Table S1. After that, the samples were named based on their experimental Ni wt% values as gCN/NiO-**X**% (**X** indicates the Ni wt%).

The morphology and structure of gCN/NiO-3.12% samples before (Figure 2a–c) and after growth of Pt NPs on them (Figure 2d,e) were characterized by transmission electron microscopy (TEM). As can be seen from Figure 2a,b, gCN shows the formation of sheets-like morphology in nanometer scale and the edges of the sheets tend to be curly.[46] In Figure 2c, the presence of the anchoring of NiO NPs with the nonuniform spherical-shaped[47] and an average diameter of about 3.5 nm on gCN nanosheets were clearly observed and pointed out by the red oval shape. The agglomeration of NiO NPs observed on gCN is most likely due to insufficient initial dispersion of precursors and increased particle mobility induced by high-temperature calcination under oxidative conditions, which collectively facilitates uncontrolled nanoparticle migration and coalescence. Additionally, Figure 2d,e shows the distribution and morphology of NiO NPs and the generated Pt NPs, on the gCN nanosheets in the gCN/NiO-Pt nanocomposites, encircled with red and green shapes, respectively. According to these TEM images of gCN/NiO-Pt nanocomposites (Figure 2d,e), the average particle size of Pt NPs was calculated to be 2.0 nm. Furthermore, Pt NPs deposition on gCN/NiO during the hydrolysis of AB caused an increase in the average particle size of NiO, which is about 4.2 nm. The presence of NiO and Pt NPs on the gCN surface was further confirmed by HAADF-STEM elemental mapping (Figure 2f–l), which indicate the co-existence of C, N, O, Ni, and Pt.

The XRD patterns of gCN/NiO nanocomposites with different Ni content (Ni wt% = 1.97, 3.12, 3.78, and 5.36) are shown in Figure 3. As a reference, the pattern of the bare gCN is also represented. For all these samples, two obvious diffraction peaks observed at 2θ = 13.1° and 27.4° were indexed to the (100) and (002) planes of gCN (**JCPDS # 87–1526**)[48] (Figure 3a). These two planes can be ascribed to the intra-planar trigonal nitrogen

© 2025 The Author(s). ChemCatChem published by Wiley-VCH GmbH

18673899, 2025, 14, Downloaded from https://chemistry-europe.onlinelibrary.wiley.com/doi/10.1002/cctc.202500419 by Koc University, Wiley Online Library on [13/11/2025]. See the Terms and Conditions (https://onlinelibrary.wiley.com/terms-and-conditions) on Wiley Online Library for rules of use; OA articles are governed by the applicable Creative Commons License

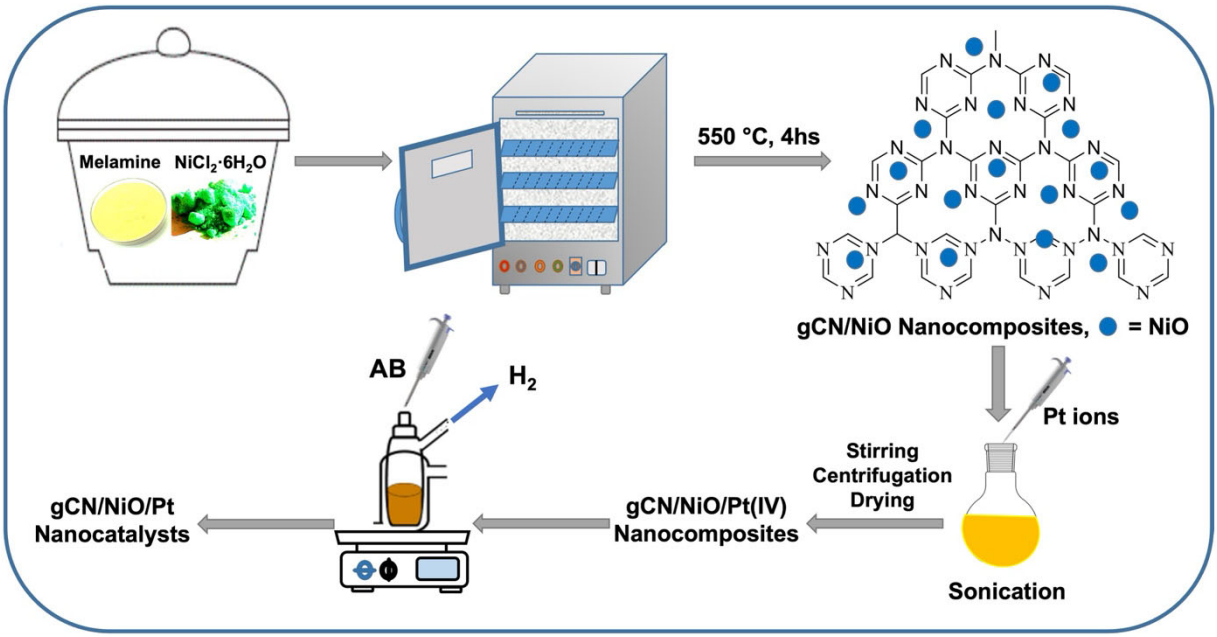


Figure 1. Schematic representation for the synthesis of gCN/NiO, gCN/NiO/Pt(IV), and gCN/NiO/Pt nanocomposites.

linkage of the tri-s-triazine units (100) and the regular packing of layers of conjugated aromatic rings (002), respectively. Although, gCN was successfully synthesized and its graphite-like structure, along with the tri-s-triazine motifs, was largely retained in the gCN/NiO composites, there is a gradual decrease in the intensity and a broadening of the (002) peak. This suggests that the incorporation of Ni atoms hinders crystal growth and inhibits the polymeric condensation of gCN.[49] In the XRD pattern of the gCN/NiO nanocomposites, the peaks appearing at $2\theta = 36.9°$, 43.1°, and 62.7° are attributed to (111), (200), and (220) planes of the face-centered cubic (fcc) NiO, respectively (**JCPDS # 47–1049**).[50] These diffraction peaks are very low in intensity and broad due to the small particle size of the NiO NPs (3.5 nm) and their very low content in the nanocomposites. Moreover, as revealed by the enlarged picture in Figure 3b, a gradual shift of the (002) peak of gCN to the lower angle with the increasing Ni content can be attributed to the increased length of the interlayer periodicity, which is related to the reaction of Ni with melamine triggering the loss of ordered structures within the gCN frameworks.[51]

The chemical states of the surface atoms of pristine gCN and gCN/NiO-3.12% nanocomposites were studied by XPS. In the survey scan XPS spectra, the presence of C, N, and O species on the surface of both gCN and gCN/NiO-3.12% were detected, while Ni is only presented in the spectrum of gCN/NiO-3.12% nanocomposites (Figure 4a). The high-resolution (HR) XPS spectra of C 1s, N 1s, and O 1s regions for gCN and gCN/NiO-3.12% are presented in Figure 4b–d, respectively. In Figure 4b, the C 1s peak from gCN was deconvoluted into the three distinct peaks at 284.5, 286.2, and 288.0 eV, which are indexed to the sp^2-hybridized carbon (**C**—[C,H]) serving as a reference, aromatic ring C bonded to terminal amino groups ((**C**)$_3$—N), and sp^2-bonded carbon (N—**C**═N) in the tri-s-triazine units, respectively.[42] Upon anchoring NiO NPs on gCN, the peaks at 286.2 and 288.0 eV are shifted toward lower binding energies, indicating the successful anchoring of the NiO NPs and their interaction with the gCN through (C)$_3$—N and N—C═O. In the N 1s spectra of gCN (Figure 4c), three peaks located at 398.5, 399.8, and 401.0 eV are observed, attributing to the sp^2-hybridized aromatic ring N (C═**N**—C), the tertiary N connecting the aromatic rings in heptazine units (**N**—(C)$_3$ or H—**N**—(C)$_2$), and terminal amino group species (**N**—H), respectively.[14] All these peaks are found to be shifted to the lower binding energies after the anchoring of NiO NPs, which is the case observed in the C 1s spectra as well. All these results verify that an electron migration occurs from gCN to NiO NPs, which signifies a significant chemical interaction between gCN and NiO NPs.[52] The O 1s spectra of gCN, presented in Figure 4d, was deconvoluted into the two peaks located at 531.5 and 532.7 eV, which are ascribed to the chemically adsorbed oxygen species or OH species and the adsorbed water molecules, respectively.[33] Apart from these two peaks, which are also showing some shifting to the lower binding energies for the O 1s spectrum of gCN/NiO-3.12% nanocomposites, there is one more peak observed at 529.1 eV, originated from the Ni—O bond, in the gCN/NiO-3.12% nanocomposites (Figure 4d).[53] In comparison with the pristine gCN, the content of the chemically adsorbed oxygen species in the gCN/NiO-3.12% nanocomposites is much higher, which indicates the presence of the more oxygen anions on the surface of the nanocomposites. Figure 4e shows the Ni 2p HR-XPS spectrum of the gCN/NiO-3.12% nanocomposites, which has the photoelectron features at 853.8/871.5 and 855.6/873.4 eV, corresponding to Ni $2p_{3/2}$ and Ni $2p_{1/2}$ core-levels of Ni^0 and Ni^{2+} species, respectively.[54] However, it should be noted that the Ni 2p spectrum is dominated by the peaks of Ni^{2+} due to the presence of greater amount of NiO in the nanocomposites. Furthermore, the co-existence of multi-electron shake-up satellite peaks at 860.8 and 879.1 are found high-resolution Ni 2p spectrum.[55] In Figure 4f, the Pt 4f

© 2025 The Author(s). ChemCatChem published by Wiley-VCH GmbH

18673899, 2025, 14, Downloaded from https://chemistry-europe.onlinelibrary.wiley.com/doi/10.1002/cctc.202500419 by Koc University, Wiley Online Library on [13/11/2025]. See the Terms and Conditions (https://onlinelibrary.wiley.com/terms-and-conditions) on Wiley Online Library for rules of use; OA articles are governed by the applicable Creative Commons License

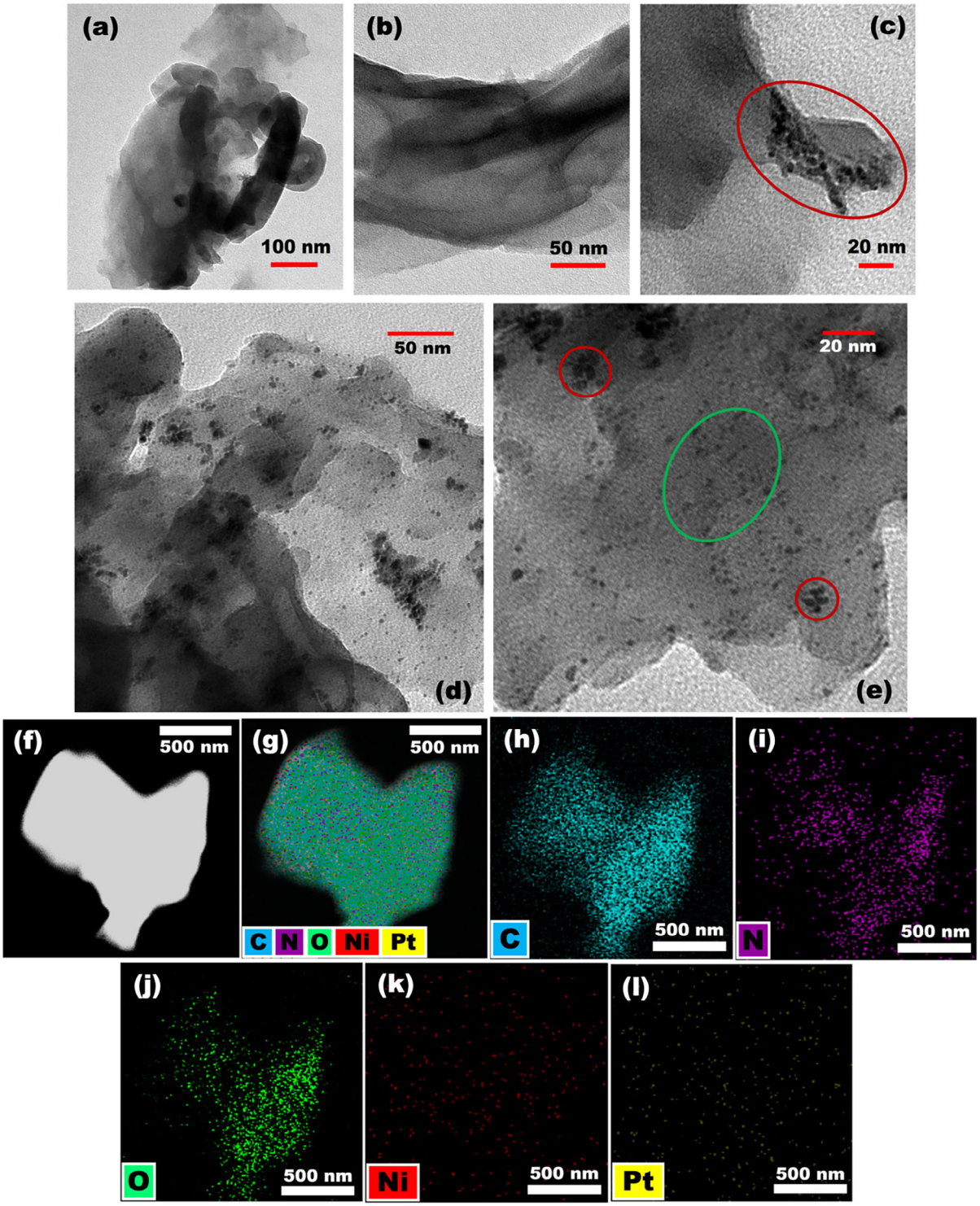


Figure 2. The representative TEM images of gCN/NiO-3.12% nanocomposites recorded at different magnifications before (a–c) and after (d, e) the generation of Pt NPs on them. HAADF-STEM image (f) of gCN/NiO-3.12%/Pt nanocomposite with elemental mapping of (g) C, N, O, Ni, and Pt, (h) C, (i) N, (j) O, (k) Ni, and (l) Pt.

HR-XPS spectrum for the gCN/NiO-3.12%/Pt nanocatalyst are shown, which proves the presence of both Pt^0 and Pt^{2+} species. The observed peaks at 71.7 and 74.9 eV are attributed to the $4f_{7/2}$ and $4f_{5/2}$ core-levels of metallic Pt (Pt^0), while the peaks at 73.3 and 76.5 eV are assigned to Pt^{2+}.[56] The strong reducing environment formed during the HAB facilitated the reduction of Pt ions and subsequently formation of Pt^0. The appearance of metallic Pt^0 confirms the in situ formation of Pt NPs, which are expected to serve as active catalytic sites for hydrogen generation from the hydrolysis of AB. On the other hand, the presence of Pt^{2+} ions, which shows the incomplete reduction of Pt precursor during the AB hydrolysis, can be attributed to

© 2025 The Author(s). ChemCatChem published by Wiley-VCH GmbH

18673899, 2025, 14, Downloaded from https://chemistry-europe.onlinelibrary.wiley.com/doi/10.1002/cctc.202500419 by Koc University, Wiley Online Library on [13/11/2025]. See the Terms and Conditions (https://onlinelibrary.wiley.com/terms-and-conditions) on Wiley Online Library for rules of use; OA articles are governed by the applicable Creative Commons License

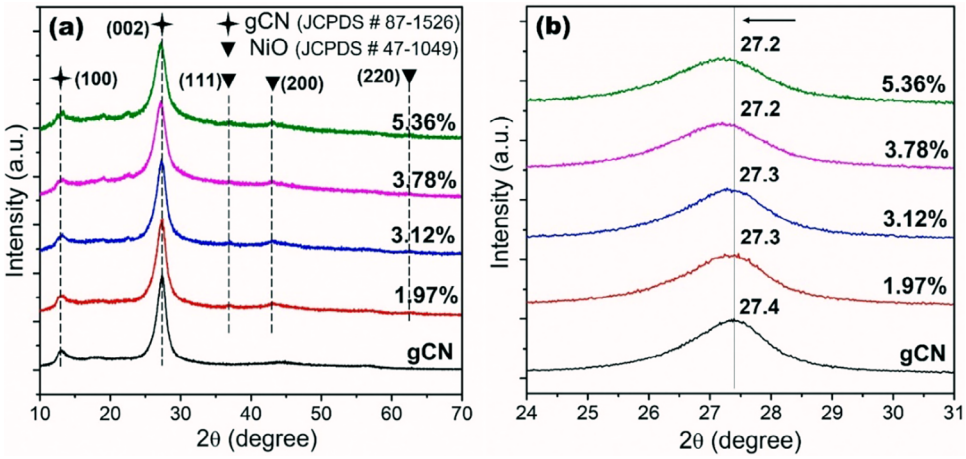


Figure 3. (a) XRD patterns of gCN and gCN/NiO nanocomposites with different Ni content (Ni wt% = 1.97, 3.12, 3.78, and 5.36) and (b) partial enlarged view of characteristic peak of gCN.

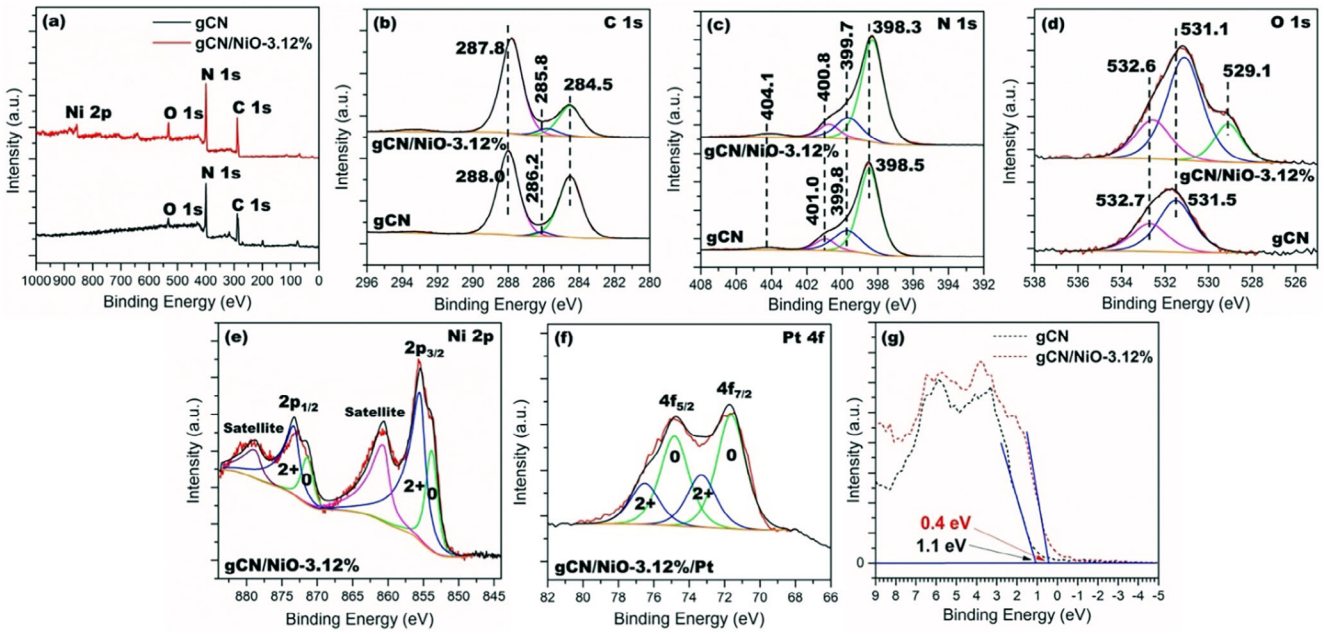


Figure 4. (a) XPS survey, HR-XPS (b) C 1s, (c) N 1s, (d) O 1s spectra of both gCN and gCN/NiO-3.12%, (e) HR-XPS Ni 2p spectra of gCN/NiO-3.12%, (f) HR-XPS Pt 4f spectra of gCN/NiO-3.12%/Pt nanocatalyst, and (g) valence band XPS spectra of gCN and gCN/NiO-3.12%.

the covalent interaction between the gCN and incorporated $[PtCl_6]^{2-}$ ions, resulting in the formation of stable Pt complexes via coordination of N-atoms with lone pairs in gCN structure.[31] Figure 4g presents the XPS valence band spectra of gCN/NiO-3.12% nanocomposites as well as of the pristine gCN. From the intersection of the linear extrapolation line to zero intensity, the leading edge of the valence band spectra of the gCN/NiO-3.12% and gCN was found to be around 0.4 and 1.1 eV, respectively, which indicates the VB shift of gCN due to the strong coupling heterostructure of gCN and NiO.

UV–vis diffuse reflectance spectra (UV–vis DRS) of all prepared photocatalysts were conducted to investigate the effect of the addition of different amount of Ni on the optical properties of pure gCN. As shown in Figure 5a, the absorption edge of the yellow powder gCN was estimated to be around 450 nm, which indicates its limited capacity to absorb visible light.[57] The red shift in the absorption edge of gCN toward the visible region becomes more visible with more amount of Ni present in the nanocomposites. Besides, the absorption intensity of the nanocomposites in the visible region is improved as the amount of Ni in the nanocomposites increases. Therefore, the visible light response of the photocatalyst is enhanced, which implies the strong interaction between gCN and NiO.[43] In addition, the band gap energies of the as-prepared nanocomposites were calculated using the Tauc plot method, where the intersection of the tangent line with the abscissa is equal to band gap energy. As illustrated in Figure 5b, the band gap energies of the gCN and gCN/NiO-X% nanocomposites with X = 1.97, 3.12, 3.78, and 5.36 Ni wt% are 2.68, 2.63, 2.63, 2.63, and 2.60 eV, respectively. As it is clearly seen, even though the increased Ni amount in

© 2025 The Author(s). ChemCatChem published by Wiley-VCH GmbH

18673899, 2025, 14, Downloaded from https://chemistry-europe.onlinelibrary.wiley.com/doi/10.1002/cctc.202500419 by Koc University, Wiley Online Library on [13/11/2025]. See the Terms and Conditions (https://onlinelibrary.wiley.com/terms-and-conditions) on Wiley Online Library for rules of use; OA articles are governed by the applicable Creative Commons License

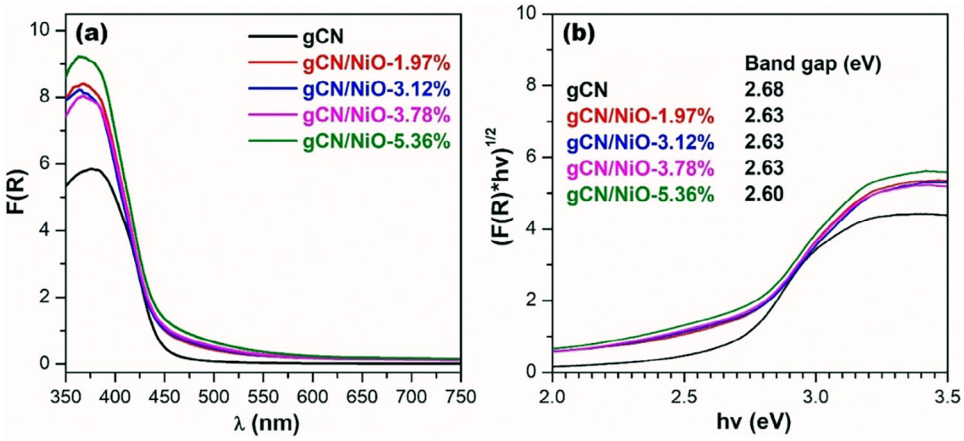


Figure 5. (a) UV–vis diffuse reflectance spectra and (b) Tauc plot of pristine gCN and gCN/NiO-X% nanocomposites consisting of 1.97, 3.12, 3.78, and 5.36 wt% Ni.

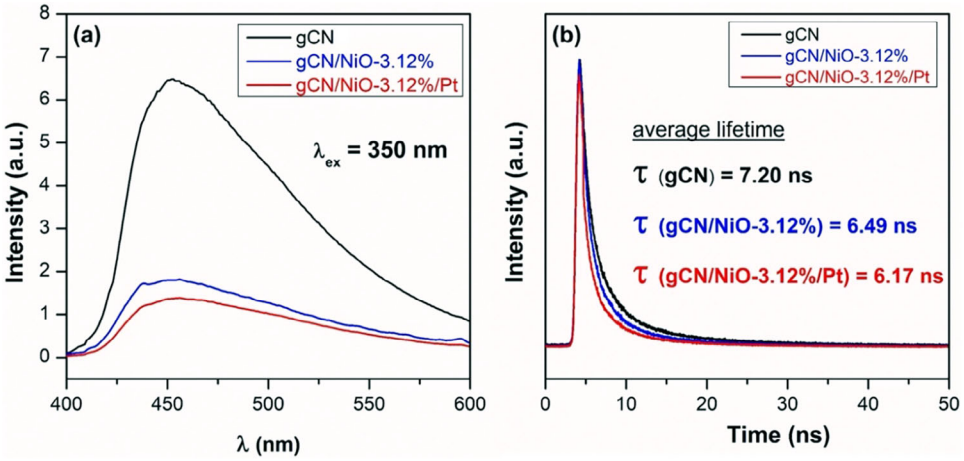


Figure 6. (a) PL spectra; (b) time-resolved emission spectra of gCN, gCN/NiO-3.12% nanocomposite and gCN/NiO-3.12%/Pt nanocatalyst.

the nanocomposites (1.97%, 3.12%, and 3.78%) resulted in the same amount of decrease in the band gap energies of nanocomposites, the decrease become clearer in the 5.36% Ni loaded nanocomposites. However, it does not mean that the nanocomposites including higher amount of Ni and having lower band gap value must perform the better photocatalytic activity in the HAB even though they absorb more light. There might be other important factors such as charge separation activity and active site concentration as well.[58]

The photoluminescence technique (PL) was conducted to compare the charge separation behavior of the gCN, gCN/NiO-3.12%, and gCN/NiO-3.12%/Pt. All materials were excited by UV light at 350 nm and the emission spectra with maxima at around 450 nm were obtained as shown in Figure 6a. The emission intensity of both gCN/NiO-3.12% and gCN/NiO-3.12%/Pt shows a sharp decline compared to the that of pristine gCN, which is attributed to the considerable prevention of charge recombination.[42] Besides, time-resolved emission spectra (TRES) of above addressed samples found to be well-fitted by the double-exponential decay function, and were indicated in Figure 6b along with the calculated average lifetime of their charge carriers. gCN/NiO-3.12% and gCN/NiO-3.12%/Pt illustrate the average lifetime of 6.49 and 6.17 ns, respectively, much shorter than that of gCN, which is 7.20 ns, referring to the existence of electron transfer channels facilitating electron transfer to the surface through the heterojunction built between the gCN/NiO and gCN/NiO/Pt.[59]

Due to the heterojunction nature of gCN/NiO-3.12% nanocomposites, which was previously approved based on its optical characterization results, the impact of white-light illumination on the HAB activity was initially tested while it was used as a support material for the growth of Pt NPs. In Figure 7a, it was approved that the hydrogen gas production via 1.31 wt% Pt loaded gCN/NiO-3.12% nanocatalyst is 1.4-fold enhanced, according to the turnover frequency (TOF) values obtained under dark and white-light irradiation (96.6 and 132.9 mol H_2 mol Pt^{-1} min^{-1}, respectively). It is worth noting that the hydrogen evolution in dark conditions is due to the inherent catalytic activity of Pt NPs, resulting in the strong affinity of Pt for B—H bond activation, leading to spontaneous hydrogen release via a thermodynamically favorable fully catalytic (non-photoinduced) pathway.[60] On the other side, integrating Pt NPs into a semiconductor heterostructure significantly enhanced the catalytic activity due to the increased electron density in the Pt

© 2025 The Author(s). ChemCatChem published by Wiley-VCH GmbH

18673899, 2025, 14, Downloaded from https://chemistry-europe.onlinelibrary.wiley.com/doi/10.1002/cctc.202500419 by Koc University, Wiley Online Library on [13/11/2025]. See the Terms and Conditions (https://onlinelibrary.wiley.com/terms-and-conditions) on Wiley Online Library for rules of use; OA articles are governed by the applicable Creative Commons License

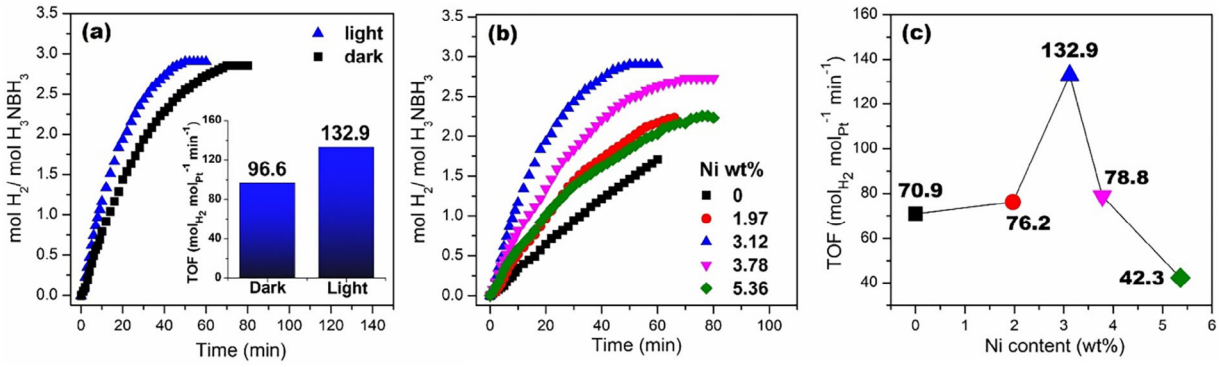


Figure 7. The plot of mol H_2/mol H_3NBH_3 versus reaction time for (a) gCN/NiO-3.12%/Pt catalyzed hydrolysis of AB conducted under irradiation of white-light and dark (the inset graph illustrates TOF values (mol H_2 mol Pt^{-1} min^{-1}) of under mentioned conditions), (b) gCN/NiO-X%/Pt with different Ni content catalyzed hydrolysis of AB conducted under irradiation of white-light. (c) The plot of TOF (mol H_2 mol Pt^{-1} min^{-1}) versus Ni content (wt%), representing the TOF values of the nanocatalysts in (b).

active sites, thus promoting more efficient B—N bond cleavage. Subsequently, the effect of Ni content in the nanocomposite on the HAB activity was examined by running experiments in the presence of theoretically 2 wt% Pt loaded gCN/NiO-X% (X: 0, 1.97, 3.12, 3.78, 5.36; X = Ni) nanocomposites (Figure 7b). Based on the ICP-MS (inductively coupled plasma- mass spectroscopy) measurement carried out after Pt ion loading on the gCN/NiO-X% nanocomposites shows that the gCN/NiO-X%/Pt(IV) with Ni wt% of 0, 1.97, 3.12, 3.78, and 5.36 contains 0.812, 1.22, 1.31, 1.33, 1.87 wt% Pt. As the amount of Ni in the nanocomposite is increasing, the amount of Pt ions anchored onto the nanocomposite is increasing too and the differences between the experimental and theoretical Pt loading amount is diminishing which might be due to the robust interaction between Pt ions and NiO. The TOF of 132.9 mol H_2 mol Pt^{-1} min^{-1} is recorded as the highest one in the presence of gCN/NiO/Pt(IV) nanocomposites including 3.12 wt% Ni and 1.31 wt% Pt. This value is 1.9 times higher than the TOF of gCN/Pt(IV) with 0.812 wt% of Pt and no Ni. This enhancement in photocatalytic activity can be attributed to the lower band gap energy and longer average charge lifespan of the gCN/NiO-3.12% heterojunction compared to gCN. At the same time, the possible Schottky junction constructed by the coupling of Pt and the semiconductors, which promotes the separation of photogenerated charges and the transfer of electrons to the surface might become more effective in the presence of NiO, as observed in the case of gCN/NiO/Pt (Figure 6).

To gain insights into the reaction mechanism of gCN/NiO/Pt under white-light irradiation, scavenger experiments were performed. $NaHCO_3$ and IPA were employed as a hole (h^+) and hydroxyl radical (•OH) scavenger, respectively.[45] As illustrated in Figure 8a, the presence of IPA caused only a slight decrease in hydrogen evolution, indicating a limited contribution of hydroxyl radicals to the overall reaction. IPA is also known as h^+ scavenger, so it is reasonable to assume that there may be a competition in scavenging hydroxyl radicals and holes to convert the isopropanol to the isopropanol radicals, expected to be less reactive than •OH radicals. Although, hydroxyl radicals may form during the process, they are not the primary oxidative species responsible for the hydrogen evolution.[61] In contrast, the addition of $NaHCO_3$ resulted in significant suppression of hydrogen production, indicating that photogenerated holes play a dominant role in sustaining efficient hydrogen release. It is also significant to mention that the photoinduced electron capture experiments performed with well-known electron scavengers, such as $Na_2S_2O_8$ and $K_2Cr_2O_7$, failed due to the facile redox reaction between the electron scavengers and AB.[38] Therefore, the scavenger experiments were performed only on photoexcited holes and hydroxyl radicals.

A possible mechanism is proposed based on the results of scavenger experiments and literature (Figure 8b). Upon white-light irradiation, photoinduced electron-hole pairs are generated on gCN. Due to the heterojunction formation between the gCN and NiO, which enhances the charge separation and prolongs the lifetime of photogenerated charge carriers, photogenerated holes preferentially migrate to the VB of NiO, while the electrons remain in the CB of gCN, which are rapidly transferred to the Pt NPs due to the favorable Schottky barrier at the gCN/Pt interface. The electrons accumulated on Pt NPs play a crucial role to weaken the electron deficient B—N bond via electron injection, resulting in the formation of $BH_3^{\delta-}$ and $NH_3^{\delta+}$ moieties. Here, the partially negative $BH_3^{\delta-}$ fragments are subsequently oxidized by photogenerated holes which are localized on NiO, leading to the evolution of H_2 gas as follows in Equation (1). Concurrently, the partially positive $NH_3^{\delta+}$ fragments can accept electrons from the Pt sites, leading to the formation of ammonium-based intermediates such as NH_4OH as follows in Equation (2). In summary, the overall photocatalytic mechanism involves the photoexcitation and charge separation, promoted by gCN/NiO interface, electron accumulation on Pt, leading to partial dissociation of ammonia borane, and the hole-driven oxidation of BH_3 species, facilitating the efficient hydrogen release.

$$BH_3^{(\delta-)} + h^+ + 2H_2O \rightarrow HBO_2 + 3H_2 \quad (1)$$

$$NH_3^{(\delta+)} + e^- + H_2O \rightarrow NH_4OH \quad (2)$$

The reaction kinetics of gCN/NiO-3.12%/Pt catalyzed hydrolysis of AB reaction were investigated in a series of experiments

© 2025 The Author(s). ChemCatChem published by Wiley-VCH GmbH

18673899, 2025, 14, Downloaded from https://chemistry-europe.onlinelibrary.wiley.com/doi/10.1002/cctc.202500419 by Koc University, Wiley Online Library on [13/11/2025]. See the Terms and Conditions (https://onlinelibrary.wiley.com/terms-and-conditions) on Wiley Online Library for rules of use; OA articles are governed by the applicable Creative Commons License

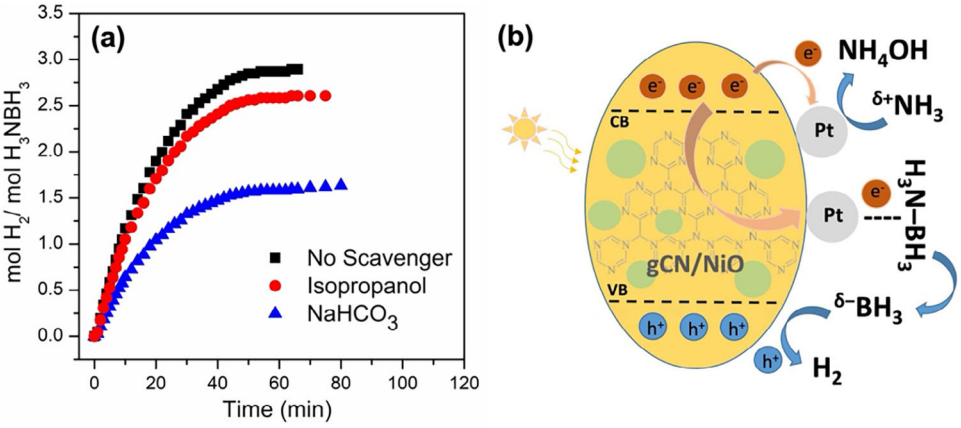


Figure 8. (a) H_2 generation versus time plots for the gCN/NiO-3.12%/Pt catalyzed hydrolysis of AB with and without scavengers. (b) Schematic illustration of the proposed photocatalytic mechanism in the presence of gCN/NiO/Pt nanocatalysts.

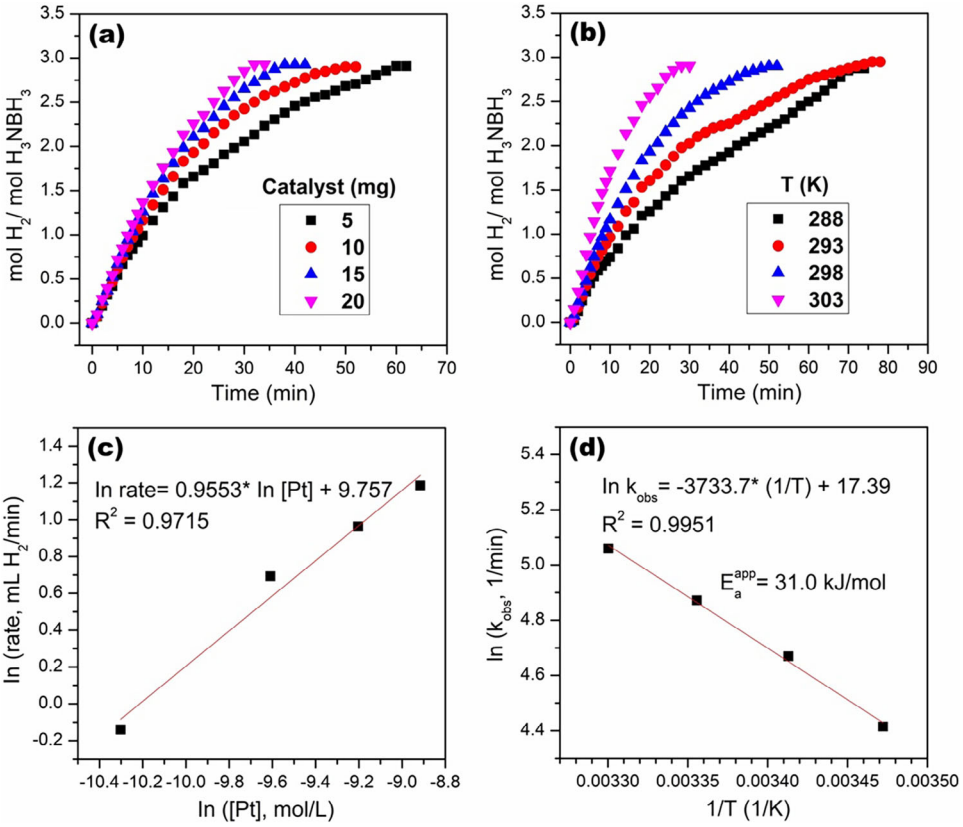


Figure 9. (a) H_2 generation versus time plots for the gCN/NiO-3.12%/Pt catalyzed hydrolysis of AB at different reaction conditions ([AB] = 0.1 M, T = 298 K, [Pt] = 0.0336–0.134 mM), (b) ([Pt] = 0.0671 mM, [AB] = 0.1 M, T = 288–303 K), (c) the plot of the logarithm of the H_2 generation rates (mL H_2/ min) versus the logarithm of [Pt], and (d) the Arrhenius plot of ln k_{obs} versus 1/T.

performed at the different gCN/NiO-3.12/-Pt amount, AB concentration, and the temperature to get the rate law and activation energy. First, the amounts of the gCN/NiO-3.12%/Pt(IV) nanocomposite were varied between 5–20 mg at a constant AB concentration (0.1 M) and temperature (298 K) and all the hydrogen generation versus time graphs were shown in Figure 9a. As the amounts of the nanocomposites were increased, the hydrogen generation rates (mL H_2/min), which are the slopes calculated from the linear portion of each plot, were increased too. In Figure 9c, the logarithm of the obtained rate values versus the logarithm of the Pt concentration (mol/L) in the nanocomposite was plotted and the slope of this plot was found to be 0.9715, proving that gCN/NiO-3.12%/Pt catalyzed HAB follows a first order reaction kinetics in regard to Pt concentration. Second, the AB amount was switched in the range of 0.5–2 mmol and the mmol of the H_2 gas produced versus time for each AB amount was illustrated in Figure S1. Based on the rate values obtained from the linear portion of each plot, a logarithmic

© 2025 The Author(s). ChemCatChem published by Wiley-VCH GmbH

18673899, 2025, 14, Downloaded from https://chemistry-europe.onlinelibrary.wiley.com/doi/10.1002/cctc.202500419 by Koc University, Wiley Online Library on [13/11/2025]. See the Terms and Conditions (https://onlinelibrary.wiley.com/terms-and-conditions) on Wiley Online Library for rules of use; OA articles are governed by the applicable Creative Commons License

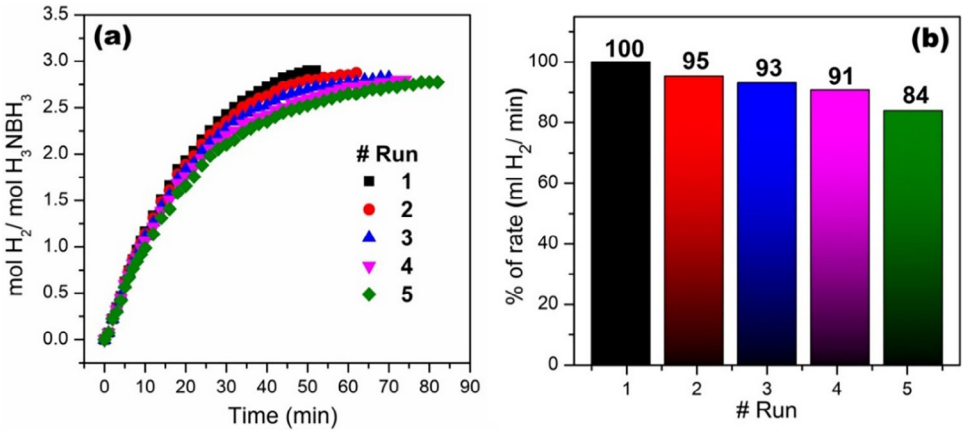


Figure 10. (a) Hydrogen generation versus time for the five times use of the gCN/NiO-3.12%/Pt nanocatalyst during the hydrolysis of AB and (b) the bar chart describing the maintained activity comparison for each following run.

graph was sketched with the H_2 generation rate (mL H_2/min) versus AB concentration (mol/L) (Figure S1). The slope of the graph is 0.048, indicating that the reaction rate does not depend on AB concentration. Accordingly, the rate law of the gCN/NiO-3.12%/Pt catalyzed HAB can be expressed as rate = k_{app}*[Pt], where k_{app} is the apparent rate constant. Finally, the temperature was varied between 288–303 K via keeping the Pt and AB concentration constant at 0.0671 mM and 0.1 M, respectively (Figure 9b) and the k_{app} (min^{-1}), which are becoming higher as the temperature is increased, was calculated for each run (Table S2). After that, the logarithm of the k_{obs} values versus inverse of corresponding temperature, 1/T (1/K), were plotted to get the Arrhenius plot (Figure 9d). According to the slope of the Arrhenius plot, the apparent activation energy (E_a^{app}) of the gCN/NiO-3.12%/Pt catalyzed HAB was found to be 31.0 kJ/mol.

The reusability of gCN/NiO-3.12%/Pt heterojunction photocatalysts during the hydrolysis of AB was tested via running five consecutive HAB experiments under white-light illumination at room temperature. The amount of H_2 produced versus time for each run was plotted in Figure 10a. Based on this, the percent of H_2 production rates versus experiment numbers were represented in a bar chart to compare the maintained H_2 production rate in each run (Figure 10b). Even though 91% of the initial activity is preserved during the fourth run, it starts to reveal a higher decrease (84%) in the activity during the fifth run. The reason of the marked decrease in the fifth run might be due to the loss of nanocatalyst in amount during the washing procedure and the decrease in the Pt wt% of the nanocatalyst during the experiment.

4. Conclusions

In summary, this study reports a facile synthesis method for the gCN/NiO nanocomposites, including Ni amounts ranging from 0 to 5.36 wt%, along with their characterization results, illustrating their efficiency in the construction of two component heterojunction structure. Subsequently, the role of gCN/NiO nanocomposites as support material for the in-situ generation of Pt NPs during the HAB under white-light irradiation were successfully examined where the 3.12 wt% Ni loaded gCN/NiO/Pt nanocomposites (1.31 Pt wt%) exhibited the highest TOF value of 132.9 mol H_2 mol Pt^{-1} min^{-1}, surpassing the performance of gCN/Pt (70.9 mol H_2 mol Pt^{-1} min^{-1}). This enhancement in activity were attributed to the significance of the heterojunction formed between gCN and NiO, enhancing visible-light absorption, photo-induced charge separation, and charge carrier transfer abilities. The kinetics studies reveal that the gCN/NiO catalyzed HAB follows a first-order reaction, dependent solely on Pt concentration, with an E_a^{app} of 31.0 kJ/mol. Remarkably, the gCN/NiO/Pt nanocatalysts demonstrates an excellent reusability, preserving 84% of its initial rate during the fifth run of HAB reaction. This work introduces gCN/NiO nanocomposites as easily synthesized and strongly coupled heterostructures, offering promising applications such as being photoactive support materials for in-situ Pt NP growth and enhanced H_2 generation from the HAB under white-light irradiation. Although, AB hydrolysis is not currently a practical route for scalable hydrogen production, it remains a valuable model reaction for the study of photocatalytic efficiency, interfacial charge dynamics, and catalyst design principles under white light irradiation. These findings contribute to the advanced photocatalytic systems for the enhancement of hydrogen production from chemical hydrogen storage compounds and moreover for other chemical transformations.

Acknowledgements

S.E.K. thanks the Scientific and Research Council of Türkiye (TUBITAK) for the scholarship in the context of 2218-Domestic Post-doctoral Research Program (Project No: 118C516). Ö.M. thanks the Turkish Academy of Sciences (TUBA) for the financial support.

Conflict of Interests

The authors declare no conflict of interest.

© 2025 The Author(s). ChemCatChem published by Wiley-VCH GmbH

18673899, 2025, 14, Downloaded from https://chemistry-europe.onlinelibrary.wiley.com/doi/10.1002/cctc.202500419 by Koc University, Wiley Online Library on [13/11/2025]. See the Terms and Conditions (https://onlinelibrary.wiley.com/terms-and-conditions) on Wiley Online Library for rules of use; OA articles are governed by the applicable Creative Commons License

Data Availability Statement

The data that support the findings of this study are available from the corresponding author upon reasonable request.

Keywords: Graphitic carbon nitride · Heterojunction · Hydrogen production · Nickel oxide · Photocatalyst

[1] K. K. Jaiswal, C. R. Chowdhury, D. Yadav, R. Verma, S. Dutta, K. S. Jaiswal, B. Sangmesh, K. S. K. Karuppasamy, *Energy Nexus* **2022**, *7*, 100118.
[2] U. Y. Qazi, *Energies* **2022**, *15*, 4741.
[3] S. K. Dewangan, M. Mohan, V. Kumar, A. Sharma, B. Ahn, *Int. J. Energy Res.* **2022**, *46*, 16150–16177.
[4] U. Eberle, M. Felderhoff, F. Schüth, *Angew. Chem. Int. Ed.* **2009**, *48*, 6608–6630.
[5] M. Yadav, Q. Xu, *Energy Environ. Sci.* **2012**, *5*, 9698.
[6] U. B. Demirci, *Int. J. Hydrogen Energy* **2017**, *42*, 9978–10013.
[7] H. Wu, Y. Cheng, Y. Fan, X. Lu, L. Li, B. Liu, B. Li, S. Lu, *Int. J. Hydrogen Energy* **2020**, *45*, 30325–30340.
[8] X. Li, J. Zhang, J. Liu, S. Wang, Y. Song, J. Zhang, *J. Alloys Compd.* **2023**, *961*, 171001.
[9] B. Coşkuner Filiz, A. Kantürk Figen, *Int. J. Hydrogen Energy* **2023**, *48*, 22954–22966.
[10] A. M. Al-Enizi, A. Yousef, M. Ubaidullah, A. Karim, M. M. El-Halwany, *J. King Saud Univ. Sci.* **2023**, *35*, 102538.
[11] J. P. Chang, C. Y. Wang, Y. J. Hsu, C. Y. Wang, *Appl. Catal. A Gen.* **2023**, *650*, 119005.
[12] H. Yang, *Mater. Res. Bull.* **2021**, *142*, 111406.
[13] M. Lin, H. Chen, Z. Zhang, X. Wang, *Phys. Chem. Chem. Phys.* **2023**, *25*, 4388–4407.
[14] H. Lin, Y. Xiao, A. Geng, H. Bi, X. Xu, X. Xu, J. Zhu, *Int. J. Mol. Sci.* **2022**, *23*, 12979.
[15] Y. Ren, D. Zeng, W. J. Ong, *Chin. J. Catal.* **2019**, *40*, 289–319.
[16] X. Yang, H. Tang, J. Xu, M. Antonietti, M. Shalom, *ChemSusChem* **2015**, *8*, 1350–1358.
[17] Y. Liu, A. Yuan, Y. Xiao, H. Yu, X. Dong, *Ceram. Int.* **2020**, *46*, 16157–16165.
[18] S. Qi, X. Liu, R. Zhang, Y. Zhang, H. Xu, *Inorg. Chem. Commun.* **2021**, *133*, 108907.
[19] Y. Orooji, M. Ghanbari, O. Amiri, M. Salavati-Niasari, *J. Hazard. Mater.* **2020**, *389*, 122079.
[20] J. Zhang, M. Zhang, R.-Q. Sun, X. Wang, *Angew. Chem.* **2012**, *124*, 10292–10296.
[21] F. Dong, Z. Zhao, T. Xiong, Z. Ni, W. Zhang, Y. Sun, W. K. Ho, *ACS Appl. Mater. Interfaces* **2013**, *5*, 11392–11401.
[22] Z. Zhao, Y. Sun, F. Dong, *Nanoscale* **2014**, *7*, 15–37.
[23] T. Selvamani, S. Anandan, M. Ashokkumar, in *Nanoscale Graphitic Carbon Nitride: Synthesis and Applications*, Elsevier, Amsterdam, the Netherlands **2022**, pp. 17–68.
[24] C. Zhou, R. Shi, L. Shang, L. Z. Wu, C. H. Tung, T. Zhang, *Nano Res.* **2018**, *11*, 3462–3468.
[25] H. Jindal, D. Kumar, M. Sillanpaa, M. Nemiwal, *Inorg. Chem. Commun.* **2021**, *131*, 108786.
[26] J. Lin, W. Tian, H. Zhang, X. Duan, H. Sun, S. Wang, *Energy and Fuels* **2021**, *35*, 7–24.
[27] C. Han, J. Li, Z. Ma, H. Xie, G. I. N. Waterhouse, L. Ye, T. Zhang, *Sci. China Mater.* **2018**, *61*, 1159–1166.
[28] C. Zhang, Y. Li, D. Shuai, Y. Shen, W. Xiong, L. Wang, *Chemosphere* **2019**, *214*, 462–479.
[29] B. Dam, B. Das, B. K. Patel, *Green Chem.* **2023**, *25*, 3374–3397.
[30] H. Kahri, M. Sevim, Ö. Metin, *Nano Res.* **2017**, *10*, 1627–1640.
[31] M. Aksoy, Ö. Metin, *ACS Appl. Nano Mater.* **2020**, *3*, 6836–6846.
[32] H. Zhang, X. Gu, P. Liu, J. Song, J. Cheng, H. Su, *J. Mater. Chem. A Mater.* **2017**, *5*, 2288–2296.
[33] M. Aksoy, S. E. Korkut, Ö. Metin, *Appl. Surf. Sci.* **2022**, *602*, 154286.
[34] S. H. Xu, J. F. Wang, A. Valério, W. Y. Zhang, J. L. Sun, D. N. He, *Inorg. Chem. Front.* **2021**, *8*, 48–58.
[35] S. H. Xu, J. F. Wang, J. P. Guo, W. Y. Zhang, A. A. U. de Souza, D. N. He, *Appl. Surf. Sci.* **2020**, *533*, 146999.
[36] S. E. Korkut, H. Küçükkeçeci, Ö. Metin, *ACS Appl. Mater. Interfaces* **2020**, *12*, 8130–8139.
[37] L. Wei, Y. Zhang, J. Liu, Y. Li, Y. Lu, H. Liu, *New J. Chem.* **2022**, *46*, 19731–19739.
[38] M. Aksoy, S. E. Korkut, Ö. Metin, *Int. J. Hydrogen Energy* **2023**, *48*, 22921–22933.
[39] C. Wang, J. Tuninetti, Z. Wang, C. Zhang, R. Ciganda, L. Salmon, S. Moya, J. Ruiz, D. Astruc, *J. Am. Chem. Soc.* **2017**, *139*, 11610–11615.
[40] X. Ren, H. Lv, S. Yang, Y. Wang, J. Li, R. Wei, D. Xu, B. Liu, *J. Phys. Chem. Lett.* **2019**, *10*, 7374–7382.
[41] U. Baig, A. Khan, M. A. Gondal, M. A. Dastageer, W. S. Falath, *Nanomaterials* **2020**, *10*, 1098.
[42] Y. X. Zhang, S. Tang, W. De Zhang, Y. X. Yu, *ACS Appl. Mater. Interfaces* **2019**, *11*, 14986–14996.
[43] L. Wang, Y. Dong, J. Zhang, F. Tao, J. Xu, *J. Solid State Chem.* **2022**, *308*, 122878.
[44] W. Gong, J. Zou, S. Zhang, X. Zhou, J. Jiang, *Electroanalysis* **2016**, *28*, 227–234.
[45] L. Wei, Y. Yang, Y. N. Yu, X. Wang, H. Liu, Y. Lu, M. Ma, Y. Chen, *Int. J. Hydrogen Energy* **2021**, *46*, 3811–3820.
[46] Y. Hong, L. Wang, E. Liu, J. Chen, Z. Wang, S. Zhang, X. Lin, X. Duan, J. Shi, *Inorg. Chem. Front.* **2020**, *7*, 347–355.
[47] M. Bonomo, *J. Nanopart. Res.* **2018**, *20*, 1–26.
[48] T. Alizadeh, S. Nayeri, N. Hamidi, *RSC Adv.* **2019**, *9*, 13096–13103.
[49] D. Das, D. Banerjee, M. Mondal, A. Shett, B. Das, N. S. Das, U. K. Ghorai, K. K. Chattopadhyay, *Mater. Res. Bull.* **2018**, *101*, 291–304.
[50] M. El-Kemary, N. Nagy, I. El-Mehasseb, *Mater. Sci. Semicond. Process.* **2013**, *16*, 1747–1752.
[51] D. Wu, K. Gao, Z. Tang, X. Zhou, F. Xie, W. Xie, X. Wang, X. Zhao, *Catal. Letters* **2021**, *151*, 3721–3732.
[52] W. Wang, B. Lv, F. Tao, *Environ. Sci. Pollut. Res.* **2023**, *30*, 25620–25634.
[53] Z. Xiao, W. Zhou, B. Yang, C. Liao, Q. Kang, G. Chen, M. Liu, X. Liu, R. Ma, N. Zhang, *Nano Mater. Sci.* **2023**, *5*, 228–236.
[54] A. M. Tarditi, N. Barroso, A. E. Galetti, L. A. Arrúa, L. Cornaglia, M. C. Abello, *Surf. Interface Anal.* **2014**, *46*, 521–529.
[55] A. M. Hengne, A. K. Samal, L. R. Enakonda, M. Harb, L. E. Gevers, D. H. Anjum, M. N. Hedhili, Y. Saih, K. W. Huang, J. M. Basset, *ACS Omega* **2018**, *3*, 3688–3701.
[56] A. Romanchenko, M. Likhatski, Y. Mikhlin, *Minerals* **2018**, *8*, 578.
[57] Z. Zhang, J. Huang, M. Zhang, Q. Yuan, B. Dong, *Appl. Catal. B* **2015**, *163*, 298–305.
[58] X. Li, Y. Chen, Y. Tao, L. Shen, Z. Xu, Z. Bian, H. Li, *Chem. Catalysis* **2022**, *2*, 1315–1345.
[59] O. Altan, Ö. Metin, *Appl. Surf. Sci.* **2021**, *535*, 147740.
[60] M. Liu, L. Zhou, X. Luo, C. Wan, L. Xu, *Catalysts* **2020**, *10*, 788.
[61] T. T. D. Nguyen, D. Nguyen, P. P. Vo, H. N. Doan, H. T. N. Pham, V. H. Hoang, K. Tien Le, K. Kinashi, V. T. Huynh, P. T. Nguyen, *J. Mol. Liq.* **2023**, *381*, 121831.

Manuscript received: March 8, 2025
Revised manuscript received: May 4, 2025
Accepted manuscript online: May 8, 2025
Version of record online: May 25, 2025

© 2025 The Author(s). ChemCatChem published by Wiley-VCH GmbH

18673899, 2025, 14, Downloaded from https://chemistry-europe.onlinelibrary.wiley.com/doi/10.1002/cctc.202500419 by Koc University, Wiley Online Library on [13/11/2025]. See the Terms and Conditions (https://onlinelibrary.wiley.com/terms-and-conditions) on Wiley Online Library for rules of use; OA articles are governed by the applicable Creative Commons License